Dalton Transactions

ROYAL SOCIETY OF CHEMISTRY

PAPER

View Article Online
View Journal | View Issue

Cite this: *Dalton Trans.*, 2025, **54**, 11588

Rare α-MoO_3–$K_2Mo_4O_{13}$ hybrid structures obtained *via* a single molecular precursor approach†

Loredana Preda,[a] Diana Visinescu, *[a] Elena Ionela Neacsu,[a] Maria Marcu,[a] Tanta Spataru,[a] Cristian D. Ene,[a] Silviu Preda,[a] Vasile-Adrian Surdu,[b] Bogdan Ştefan Vasile,[b] Roxana Doina Truşcă,[b] Adrian-Ionuţ Nicoară,[b] Elena Mirabela Soare,[a] Maria-Gabriela Alexandru *[c] and Adelina-Carmen Ianculescu[b]

Rare K/Mo-based hybrid structures were obtained through a new approach, employing the 4d cyanometallate complex, $K_4[Mo^{IV}(CN)_8]$, as a new single molecular precursor. The dissociation of the $K_4[Mo^{IV}(CN)_8]$ complex, under hydrothermal conditions, led to the dark-brown amorphous material **P**. The subsequent calcination of **P** gave rise to the light-yellow crystalline products **1** (at 400 °C) and **2** (at 500 °C). The XRD data and Rietveld analysis revealed that **1** and **2** consist of a mixture of two crystalline phases: orthorhombic α-MoO_3 and triclinic $K_2Mo_4O_{13}$, in close percentages, with a prevalence of the molybdenum oxide phase. *In situ* XRD experiments up to 630 °C showed that the thermal conversion of **P** results in the formation of the α-MoO_3–$K_2Mo_4O_{13}$ mixture, in which α-MoO_3 grows along the (0*k*0) direction, as the temperature increases, whereas the triclinic $K_2Mo_4O_{13}$ phase melts at 520° C. These results were confirmed by the *in situ* Raman experiments on **P**. The FE-SEM analysis revealed a temperature-dependent morphology: the fused quasi-spherical aggregates of very small nanoparticles of **P** (up to 10 nm) were converted into large conglomerates comprising a mixture of fused rods/prisms of α-MoO_3 and nano- and sub-micron sized polyhedral-type $K_2Mo_4O_{13}$ particles for **1**, and, for **2**, into well-separated phases of α-MoO_3 micro-particles with a 1D morphology and sub-micron polyhedral particles of potassium tetramolybdate. For **2**, HR-TEM investigations revealed details of a complex self-assembly mechanism of the elongated particles of molybdenum oxide into 1D hierarchical structures (belts, rods and thick prisms). The capacitive features of the graphite-electrodes modified with **P**, **1** and **2** materials, as well as with a mixture of graphene and **2** were investigated.

Received 4th May 2025,
Accepted 29th June 2025

DOI: 10.1039/d5dt01044f

rsc.li/dalton

Introduction

Molybdenum oxides, MoO_x ($2 \leq x \leq 3$), represent a rich and versatile family of Mo-based materials with n-type semi-conducting properties and showing various structures, morphologies and compositions[1] that, further, trigger different physicochemical properties of interest in (photo)catalysis,[2,3] photochromism,[4] and cytotoxicity[5,6] as well as in electrochemical applications.[7,8] Focusing on the polymorphic and stoichiometric molybdenum(VI) oxide, the orthorhombic α-MoO_3 represents the most thermodynamically stable crystalline phase, with an anisotropic double-layered structure of corner- and edge-sharing MoO_6 octahedral building units, growing along the [100] and [001] directions, that further generates 1D morphologies like wires,[9,10] fibers,[11] rods, or belts.[11,12] Such 1D morphologies are particularly appealing for electrochemical applications due to the large electrode–electrolyte contact area, facile strain relaxation and efficient 1D electron transport pathway. Also, the bi-layered structure of

[a]*Institute of Physical Chemistry - Ilie Murgulescu, Romanian Academy, 202 Splaiul Independentei, 060021 Bucharest, Romania. E-mail: diana.visinescu@gmail.com*
[b]*Department of Science and Engineering of Oxide Materials and Nanomaterials, National University of Science and Technology Politehnica Bucharest, Bucharest, 060042, Romania*
[c]*Department of Inorganic Chemistry, Physical Chemistry and Electrochemistry, Faculty of Chemical Engineering and Biotechnologies, National University of Science and Technology Politehnica Bucharest, 1-7 Gh. Polizu Street, 011061 Bucharest, Romania. E-mail: maria.alexandru@upb.ro*

† Electronic supplementary information (ESI) available: FTIR spectra of **P**, **1** and **2** (Fig. S1), NIR-UV-Vis spectra and Tauc plots of **1** and **2** (Fig. S2 and S3), PL spectra of **1** and **2** (Fig. S4); TG-DTG-DSC plots of **P** (Fig. S5), XRD patterns of **P**, **1** and **2** (Fig. S6 and S7), Rietveld diagrams for **1** and **2** (Fig. S8), *in situ* XRD patterns of **P** (Fig. S9), FE-SEM images of the cooled sample of **P** after thermal treatment at 630 °C (Fig. S10); *in situ* Raman spectra of **P** between 50 and 100 °C (Fig. S11), FE-SEM image and EDX elemental mapping and spectrum of **P** (Fig. S12), FE-SEM image and EDX spectra on a selected region of the rod-like particle of **1** (Fig. S13), FE-SEM image and EDX maps of **1** (Fig. S14), FE-SEM image and EDX spectrum and maps of **2** (Fig. S15), CV plots for **2**/**G** (Fig. S16a) and **2**-**Gr**/**G** (Fig. S16b) at sweep rates ranging from 5 up to 200 mV s^{-1} (Fig. S16), GCD curve for **P**/**G** at j = 0.07 A g^{-1} (Fig. S17), and FE-SEM images of **2**/**G**- and **2**-**Gr**/**G**-modified electrodes (Fig. S18). See DOI: https://doi.org/10.1039/d5dt01044f

α-MoO_3 can host Li^+, Na^+ or K^+ cations, which makes it a suitable electrode for Li/Na/K-ion batteries or for charge storage applications.[13–16]

The molybdenum-based hybrid structures assembled from α-MoO_3 and alkaline/transition metal-containing molybdates ($A_2M_4O_{13}$ for A^+ = Li, Na and K; $MMoO_4$ for $M^{2+,3+}$ = Cr, Mn, Fe, Co, Ni, Cu, or Zn) represent a new family of materials that emerged in the last decade, especially due to their excellent catalytic wet air oxidation (CWAO) properties.[17,18] Besides, uniform rod-like α-MoO_3 particles mixed with 2.3% $K_2Mo_4O_{13}$ showed very good electrochemical properties in lithium-ion batteries (LIBs), as well as pseudo-capacitance in sodium-ion batteries (SIBs),[19] highlighting the benefits of such a composition in charge storage applications. Surprisingly, despite their promising features, the α-MoO_3–$K_2Mo_4O_{13}$ hybrid structures were rarely reported, being obtained by thermal decomposition of hydrated potassium bronze, $K_{0.23}MoO_3(H_2O)_{0.43}$,[20] through a hydrothermal (HT)[18] or sonochemical method,[19] or through a two-step precipitation/calcination process.[21] The SEM morphological analysis of several examples showed, in all cases, only a fused structural arrangement of alpha-molybdenum oxide and Na/K tetramolybdate components.[18,19,21] Therefore, the development of efficient and, also, scalable methods for obtaining α-MoO_3–$K_2Mo_4O_{13}$ hybrids is very important for enriching this restrained series of hybrid materials with new examples with fine-tuned composition and morphostructural characteristics.

Coordination compounds are increasingly being used as single molecular precursors of metal oxides, providing suitable routes to prepare pre-designed nanomaterials at the molecular level.[22] The advantages of this approach are related to the simple, accessible synthetic procedure, and well-defined crystalline compounds as precursors, which can be tuned/modified to adjust the obtained material structure correlated with its functionality. HT treatment of iron(II)/iron(III) hexacyanometallates led to diverse nano- and microstructures of iron oxide polymorphs.[23–26] More recently, the calcination of cyano-bridged $M^{II}[Mo(CN)_8]\cdot xH_2O$ (M = Co, Fe) 3-D coordination polymers generated hollow octahedra of Co_3O_4/$CoMoO_4$[27] or micro-octahedra of the MoO_3–Fe_2O_3 mixture of oxides,[28] which were studied as anodes for LIBs. These last results opened interesting possibilities in the chemistry of 4d oxide materials by introducing new types of cyano-based molybdenum molecular precursors.

The aqueous dissociation of cyanometallate complexes of 4d/5d metal analogues, such as octacyanometallate(IV) complexes, $K_4[M(CN)_8]$ [M^{IV} = Mo, W], under hydrothermal conditions, to afford the corresponding Mo/W oxide-based materials has not been explored to date. The Mo^{IV}/W^{IV} cyano complexes exhibit a variety of distorted coordination geometries (dodecahedral, D_{2d}, or square antiprism, D_{4d})[29] and the aqueous solution of $K_4[Mo^{IV}(CN)_8]$ is photosensitive due to the redox lability of the molybdenum species.[29] All these features recommend $K_4[Mo^{IV}(CN)_8]$ as a well-suited starting material for Mo-based oxide materials.

Molybdenum (metal powder), peroxomolybdic acid and ammonium heptamolybdate represent the typical sources of Mo-based oxide materials through HT synthesis. However, the procedure usually requires chemical pre-treatment with H_2O_2 or nitric acid.[30–32] Inspired by the success of hexacyanoferrates in the synthesis of iron(II, III) oxide particles,[23–26] we employed potassium octacyanomolybdate(IV) as a single molecular precursor of Mo-based nano- or micro-sized oxide materials. Moreover, the simultaneous presence of potassium and molybdenum ions has the potential to generate K/Mo-based oxide hybrid structures.[18]

Herein, we describe the one-step synthesis of hybrid structures obtained *via* the hydrothermal treatment of an aqueous solution of $K_4[Mo^{IV}(CN)_8]$ in the absence of a surfactant: amorphous pristine material, denoted as **P**, a hydrated K/MoO_x hybrid material, and its subsequent calcination at 400 and 500° C, respectively, comprising a mixture of two crystalline phases, α-MoO_3 and $K_2Mo_4O_{13}$, labelled as **1** (400° C) and **2** (500° C). The composition, crystallinity and morphologies of **P**, **1** and **2** are influenced by the calcination temperature. In-depth morphostructural analyses of **P**, **1** and **2**, including the *in situ* XRD and Raman spectroscopy experiments to survey the thermal behavior of **P** and its conversion into **1** and **2**, were carried out. Additionally, the capacitive behavior of **P**, **1** and **2** was mainly investigated through cyclic voltammetry (CV) and galvanostatic charge–discharge (GCD) tests.

Experimental

Materials and synthesis

The starting material $K_4[Mo^{IV}(CN)_8]\cdot 2H_2O$ was prepared as outlined in the literature.[33] Nafion 117 was obtained from Sigma-Aldrich. *N*-Methyl-2-pyrrolidone (NMP) solvent (99.8%, Roth) of analytical grade was used without further purification.

Synthesis of P, 1 and 2. The aqueous solution (0.83 g, 30 mL) of $K_4[Mo^{IV}(CN)_8]\cdot 2H_2O$ was sealed in a 45 mL capacity autoclave and was heated at 150 °C for 60 h. The as-obtained dark-brown product (**P**) was collected by centrifugation, washed with double distilled water and ethanol, and dried under vacuum. Compound **P** was subsequently calcined in air at 400 (**1**) and 500 °C (**2**), respectively, for 1 h, to afford light-yellow products, **1** and **2**, respectively.

Thermal investigations. The thermal analysis was carried out in alumina crucibles, under static air, with a sample mass of *ca.* 10 mg at a heating rate of 5 K min^{-1} on a NetzchSTA 409 PC/PG thermobalance.

Spectral investigations. The IR spectra (KBr pellets) were recorded in the 4000–400 cm^{-1} range with a FTIR Bruker Tensor V-37 spectrophotometer. NIR-UV-Vis spectra (diffuse reflectance technique) were recorded in the 200–1800 nm range with a JASCO V-770 spectrophotometer, using MgO as the standard. Photoluminescence (PL) measurements were performed on a JASCO FP 8300 spectrophotometer using 320 nm excitation line of xenon light.

(*In situ*) Raman experiments were performed using a Jobin Yvon T64000 spectrometer equipped with a cooled charge-coupled device detector. The backscattering geometry was

used for analysing the scattered light. The spectral excitation was provided by an Ar^+ laser using the 514.5 nm laser line. Very low power laser density was used to avoid overheating the sample with the laser beam. The slits were set for a spectral resolution of 2 cm^{-1}.

Structural and morphological investigations

X-ray diffraction analysis. Powder X-ray diffraction (XRD) patterns were collected at room temperature using the theta–theta geometry on a PANalytical Empyrean X-ray diffractometer, with CuKα radiation (λ = 1.5418 Å) operating at 45 kV and 40 mA. Counts were collected in the 2θ range of 10°–80°, with a step size of 0.02° and time per step of 255 seconds with a PIXCel3D detector operated in the line scanning mode. PXRD data were analysed using HighScorePlus 3.0 e software, with a whole pattern profile fitting (WPPF) module, connected to the ICDDPDF4+ database. Crystallite size D, micro-strains and unit cell parameters were estimated from the PXRD data using the Rietveld refinement method.

(*In situ*) XRD experiments. Qualitative *in situ* powder XRD was measured under an open air atmosphere in continuous mode in the temperature range from room-temperature up to 630 °C on a Rigaku Ultima IV diffractometer in the θ–θ mode using Cu-Kα radiation (1.5418 Å) at a fixed power source (40 kV and 30 mA). Data were collected in the 2θ range of 10–60°, at a step size of 0.02° and a scan rate of 1° min^{-1}. Phase identification was performed using Rigaku's PDXL software connected to the ICDD PDF-2 database.

Scanning/transmission electron microscopy (SEM/TEM) and high resolution-transmission electron microscopy (HR-TEM) analyses. To analyse the oxide particle size, morphology, and crystallinity degree and to check the chemical composition, purity and chemical homogeneity, SEM, TEM and HR-TEM coupled with SAED (selected area electron diffraction) and EDX (energy dispersive X-ray spectroscopy) investigations were performed using a high-resolution FEI QUANTA INSPECT F scanning electron microscope (FE-SEM) with a field emission gun and a Tecnai™ G^2 F30 S-TWIN transmission electron microscope (TEM/HR-TEM) from Thermo Fisher Scientific. The settings used for the SAED investigation were: diffraction mode and image size of 2048 × 2048 pixels with a pixel size of 0.095 × 1 nm^{-1} × 0.095 × 1 nm^{-1} at a magnification of 750 and 300 kV accelerating voltage. For the acquisition of the EDX spectra and elemental maps, the transmission electron microscope was operated in STEM (scanning transmission electron microscopy) mode at 300 kV using a HAADF (high-angle annular dark-field) detector for imaging and an in-column windowless 4 Super EDX detector for elemental analysis.

Electrochemical measurements

The electrochemical investigations were carried out in a standard three-electrode glass cell, at room temperature, in 0.5 M Na_2SO_4 as an electrolyte with a potentiostat/galvanostat PARSAT 4000. An Ag/AgCl electrode and a platinum wire were employed as the reference and counter electrodes, respectively. The pristine **P** compound and its calcined products **1** and **2** (*ca.* 2.5 mg) were each mixed with 15 μL of Nafion solution (5%) and 100 μL of *N*-methyl-2-pyrrolidone (NMP). These three different inks were each uniformly deposited on graphite plate (**G**) substrates and the coated electrodes, labelled **P/G**, **1/G** and **2/G**, were further dried at 60 °C for 5 h. Following the same steps, the graphite plates were also modified with a mixture of compound **2** and graphene (**Gr**) (20% graphene and 80% compound **2**) and the obtained electrode was denoted as **2-Gr/G**. For comparison, graphite electrodes were also modified with graphene (**Gr/G**). These modified electrodes were employed as working electrodes and their geometric surface area was *ca.* 1 cm^2. The electrochemical characterization of all samples was performed by using cyclic voltammetry (CV), galvanostatic charge–discharge (GCD) and electrochemical impedance spectroscopy (EIS) techniques. The cyclic voltammograms were recorded at different sweep rates (5–200 mV s^{-1}), and the charge discharge curves were recorded at different current densities (*i.e.* between 0.166 A g^{-1} and 1 A g^{-1}) over a potential range where their capacity of storage charge is significant. The EIS tests were carried out at the open circuit potential (OCP) in the frequency range between 10 mHz and 100 kHz with an amplitude of an alternating signal of 5 mV. The ZSwimWin 3.21 software was used for fitting the impedance spectra. Three identical samples of each electrode were tested to confirm the reproducibility.

Results and discussion

The HT treatment of an aqueous solution of the $K_4[Mo^{IV}(CN)_8]$ complex at 150 °C for 60 h, in the absence of any additive, afforded the amorphous dark-brown product **P**. The post-synthetic calcination treatments of **P** at 400 and 500 °C generated the light-yellow crystalline powders of **1** (400 °C) and **2** (500 °C), and the samples were preliminary analysed through FTIR and NIR-UV-Vis spectroscopy (for **1** and **2**). Solid-state photoluminescence (PL) measurements were performed at room temperature on **1** and **2** to reveal the surface and/or intrinsic defects of the hybrid materials. Also, the thermal behaviour of **P** was investigated through TG-DTG-DSC analysis.

Preliminary characterization

FTIR spectra of P, 1 and 2. The infrared spectra for **P**, **1** and **2** shown in Fig. S1 in the ESI† reveal two broad, structured, and intense absorptions that cover the 1000–800 cm^{-1} and 800–400 cm^{-1} range for all compounds. For the pristine compound **P**, the bands are less delimited with peaks at 950/906 cm^{-1} and 698/597 cm^{-1}, whereas for the calcined products **1** and **2**, sharp peaks occur. For **1** and **2**, the bands at *ca.* 990 cm^{-1} could be assigned to the stretching vibration of the terminal Mo=O bond in the orthorhombic α-MoO_3 phase. Also, for **1**, the band at *ca.* 890 cm^{-1} could be attributed to the Mo–O–Mo vibrations, which was red shifted for **2** (peak at *ca.* 869 cm^{-1}), most likely due to a change of the morphology.[34] Additional bands appear both for **1** and **2** at 945, 746, 620 and 515 cm^{-1}, which correspond to ν_{asym}(Mo=O) and ν_{st}(Mo–O–

Mo) vibrations in a secondary, co-existent potassium tetramolybdate phase.[35,36] The peaks in the 700–400 cm^{-1} region arise from the bending vibrations of the Mo–O–Mo fragment belonging to the α-MoO_3 phase. For **P**, the FTIR spectrum indicates the formation of an incipient hydrated K/MoO_x phase, based on the broad bands at 3455 and 3160 cm^{-1} (O–H stretching vibrations), and the band at *ca.* 1630 cm^{-1} ascribed to the bending mode of hydroxyl groups.

The calcined samples, **1** and **2**, were also investigated through diffuse reflectance spectroscopy that provides information about the band gap of the two compounds. The overlapped NIR-UV-Vis spectra for **1** and **2** are shown in Fig. S2 in the ESI.† Both samples show strong bands in the UV region at 322 and 330 nm with a shoulder at 260 nm, which originates from the charge transfer of the Mo–O moiety in the MoO_6^{6-} octahedron.[34] Fig. S3 in the ESI† displays the overlaid Tauc plots ($(\alpha h\nu)^2$ *vs.* $h\nu$) for **1** and **2** based on which the energy band gap, E_g, was determined by extrapolating the linear region in the plots. The values for E_g of 2.82 eV for **1** and 2.67 eV for **2** were smaller than the value for bulk molybdenum oxide of 3.2 eV, which could be caused either by the change of the morphostructural properties and/or the co-existence of a potassium molybdate secondary phase (with E_g = 1.9 eV).[35,36] The smaller band gap value for **2** most probably results in higher conductivity of this compound, beneficial for electrochemical applications. Both **1** and **2** show a broad absorption in the 800–1100 nm range attributed to the localized surface plasmon resonance phenomenon.[37] The overlapped PL spectra of **1** and **2** are presented in Fig. S4 in the ESI† exhibiting similar shapes with a strong UV emission at around 354 nm as well as a broad visible emission with multiple shoulders in the violet-blue region (405, 435 and 450 nm) of the spectra. Weak intensity peaks occurred also in the green-yellow region at 550, 570 and 600 nm. The strong UV emission is located closer to the near band edge (NBE) emission of the bulk molybdenum oxygen (3.2 eV) and can be attributed to the free exciton recombination. Also, the visible peaks could be tentatively assigned to the deep level emissions and have multiple causes: oxygen vacancies, the co-existent $K_2Mo_4O_{13}$ phase and/or interstitial Mo or surface defects.[38]

Thermal analysis was performed for **P**; the TG-DTG-DSC plots are displayed in Fig. S5 in the ESI.† The TG curve of **P** shows an initial weight loss of *ca.* 10% up to 100° C corresponding to the removal of the water molecules and a broad plateau between 100 and 700° C that indicates the formation of a stable product. The broad, three-structured DSC exothermic peak with shoulders at 330 and 410 °C points out a phase transition related to the simultaneous crystallization of the two different phases, orthorhombic α-MoO_3 and triclinic $K_2Mo_4O_{13}$. The sharp endothermic peak from 520 °C is attributed to the melting process of the tetramolybdate phase, whereas the melting of α-MoO_3 appears as a broad endothermic peak at *ca.* 720 °C.

Structural investigations

All samples, **P**, **1** and **2**, were structurally investigated through powder X-ray diffraction. The pristine **P** compound proved to be amorphous (see Fig. S6 in the ESI†), whereas the diffraction patterns were similar for **1** and **2** (Fig. S7 in the ESI†), both revealing the co-existence of two crystalline phases: α-MoO_3 (orthorhombic *Pnma*, ICCD 01-086-8446) and potassium tetramolybdate $K_2Mo_4O_{13}$ (triclinic, $P\bar{1}$, ICCD04-014-3555).[1,39,40] Although the XRD patterns are similar, the intensities of the peaks attributed to the (020), (040) and (060) planes for **2** increase compared to **1**. Most likely, a higher calcination temperature determines an increase in the frequency of the appearance of crystalline (0*k*0) planes and a preferential growth along the *y* direction of a large proportion of the α-MoO_3 crystalline phase crystals.[41] Rietveld analysis allowed the determination of the proportion of the two crystalline phases and their corresponding structural parameters (Table 1).

Table 1 The structural characteristics and the fitting parameters obtained by the Rietveld refinement for **1** and **2**

Sample symbol	**1** (400 °C)		**2** (500 °C)	
Phase composition	MoO_3	$K_2Mo_4O_{13}$	MoO_3	$K_2Mo_4O_{13}$
Amount (%)	58.8	41.2	54.9	45.1
ICDD PDF4+	01-086-8446	04-014-3555	01-086-8446	04-014-3555
a (Å)	13.8738 ± 0.0010	7.9392 ± 0.0009	13.8633 ± 0.0007	7.9376 ± 0.0010
b (Å)	3.6953 ± 0.0002	8.3383 ± 0.0010	3.6972 ± 0.0001	8.3418 ± 0.0011
c (Å)	3.9612 ± 0.0003	10.0034 ± 0.0013	3.9627 ± 0.0002	10.0058 ± 0.0014
Crystal system	Orthorhombic	Triclinic	Orthorhombic	Triclinic
Space group	*Pnma*	$P\bar{1}$	*Pnma*	$P\bar{1}$
α (°)	90	107.04	90	107.0397
β (°)	90	102.8453	90	102.8393
γ (°)	90	109.6386	90	109.6508
Volume, *V* (Å^3)	203.084	557.196	203.110	557.406
R_{exp} expected	4.1754		4.3478	
R_p profile	5.9829		5.4495	
Weighted R_{wp} profile	10.6940		8.6407	
Goodness of fit, χ^2	6.5598		3.9496	
Crystallite size, $\langle D \rangle$ (nm)	40.23 ± 15.35	50.38 ± 14.55	75.73 ± 10.83	45.91 ± 9.65
Micro-strain, $\langle S \rangle$ (%)	0.20 ± 0.03	0.15 ± 0.01	0.09 ± 0.01	0.18 ± 0.03
Crystallinity (%)	44.82		47.52	

The increase of the calcination temperature leads to: (i) a slight increase of the proportion of the secondary $K_2Mo_4O_{13}$ phase at the expense of the major MoO_3 phase, (ii) the increase of the unit cell volume, *V*, especially for the $K_2Mo_4O_{13}$ phase, whose unit cell expansion is almost three times higher compared to that of MoO_3 and (iii) the significant increase of the average crystallite size, $\langle D \rangle$, for the MoO_3 phase relative to that of $K_2Mo_4O_{13}$, which is almost thermally invariant taking into account the error bars, contributing to an overall enhancement of the crystallinity degree (Table 1). The superimposed plots of the experimental and calculated XRD patterns of **1** and **2** are comparatively presented in Fig. S8(a) and (b) in the ESI.†

The effect of the preferred orientation was incorporated into the Rietveld refinement procedure using the March Dollase formalism,[42] which corrected the diffracted intensities of α-MoO_3 along the (010) family of crystallographic planes during the fit of the patterns. The March *r* parameter controls the distribution shape and is an index of the extent of preference in orientation, *r* being unity for an ideal random-orientation XRD data. The *r* parameter for **1** that was calcined at 400 °C was found with the value 0.89 ($r < 1$), which is specific to foil-/plate-like crystals (2D morphology), packing along the diffraction vector. In the case of **2**, the *r* parameter had a value of 1.04 ($r > 1$), which is specific to rod-like crystals (1D morphology).[43]

However, the crystallization process and the evolution of the two crystalline phases is best surveyed by carrying out *in situ* XRD experiments (see Fig. S9 in the ESI†) on the pristine **P** material from room temperature up to 630 °C. Several important conclusions could be outlined following this study:

(i) The Mo-containing phases start to crystalize above 330 °C, a process that is also supported by the broad exothermic DSC peak in the 300–450 °C temperature range (Fig. S5 in the ESI†), assigned to phase transitions and the gradual crystallization of the orthorhombic α-MoO_3 and triclinic $K_2Mo_4O_{13}$.

(ii) The peaks related to the (0*k*0) plane follow a similar trend observed for the room temperature XRD patterns of **1** and **2**, increasing in intensity from *ca.* 450 up to 590 °C, which reveals a preferential growth along the *y* axis of the α-MoO_3 1-D structure. Nevertheless, the (0*k*0) peaks clearly diminish in intensity at 630 °C likely due to a change of the morphology of the orthorhombic α-MoO_3 (see Fig. S10 in the ESI†).

(iii) The increase of the calcination temperature above 450° C causes a gradual disappearance of the peaks attributed to potassium tetramolybdate (the melting point of the bulk $K_2Mo_4O_{13}$ is 546 °C), the XRD pattern from 530 °C corresponding to a single crystalline phase of α-MoO_3. Besides, the sharp endothermic peak from the DSC curve of **P** confirms the melting process of the tetramolybdate phase at *ca.* 520 °C.

To support the conclusions based on the XRD data, room temperature Raman spectroscopy and *in situ* Raman experiments from room temperature up to 550 °C were carried out on **P** (Fig. 1 and Fig. S11 in the ESI†). The Raman spectra show well-defined peaks corresponding to the α-MoO_3 and triclinic

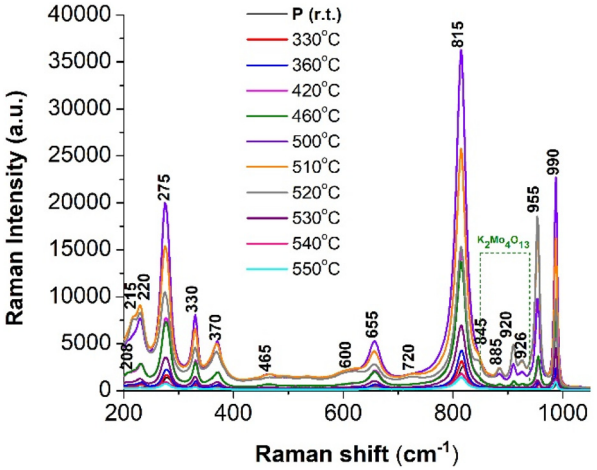

Fig. 1 *In situ* Raman spectra of pristine **P** at temperatures ranging from room temperature up to 550 °C. The green dashed lines indicate the region of bands assigned to the $K_2Mo_4O_{13}$ crystalline phase.

$K_2Mo_4O_{13}$ phases. The medium and strong intensity peaks at 660, 815 and 990 cm^{-1} correspond to the ν(O–Mo–O), B_{2g}/B_{3g}, ν_s(Mo═O), A_g/B_{1g}, and ν_{as}(Mo═O), A_g/B_{1g} vibrations, respectively, for the orthorhombic MoO_3 phase.[44,45] The bands at 382 and 367 cm^{-1} are assigned to the δ(O–Mo–O) scissoring, while the band at 338 cm^{-1} is assigned to the δ(O–Mo–O) deformation in α-MoO_3.[46] The Raman bands located at 280 cm^{-1} (B_{2g}) and 288 cm^{-1} (B_{3g}) are assigned to the bending vibrations δ(Mo═O). These values and the band intensity ratio are close to those reported for nanorod- and nanobelt-shaped α-MoO_3 materials, growing along a preferential direction.[47,48] Some of the bands exhibited in the Raman spectrum by the $K_2Mo_4O_{13}$ crystalline phase are masked by the α-MoO_3 bands. The tetramolybdate phase is characterized by bands at 958, 918 and 892 cm^{-1}, generated by the $\nu(MoO_2)$, $\nu(MoO_3)$, and ν(MoOMo) vibrations, respectively, that are absent in the orthorhombic molybdenum trioxide Raman spectrum.[49,50]

The calcination of **P** leads to an increase of the peak intensities attributed to the two crystalline phases, the highest intensity occurring at 500 °C, for α-MoO_3 bands, and at 520 °C for $K_2Mo_4O_{13}$. However, above 520 °C, the gradual disappearance of the tetramolybdate characteristic bands corresponds well to the XRD and thermal analysis data that indicate the melting of $K_2Mo_4O_{13}$. Thus, both α-MoO_3 and tetramolybdate phases simultaneously crystallize and co-exist up to 520 °C.

Morphological analysis

The morphology of **P**, **1** and **2** was analysed through FE-SEM (Fig. 2–4 and Fig. S12–S15 in the ESI†) and TEM (HR-TEM) investigations (Fig. 5 and 6).

The low-magnification FE-SEM image of **P** shows the formation of almost spherical micro-aggregates (Fig. 2(a)). The detailed higher-magnification images indicate an obvious structuring of these amorphous aggregates, which consist of

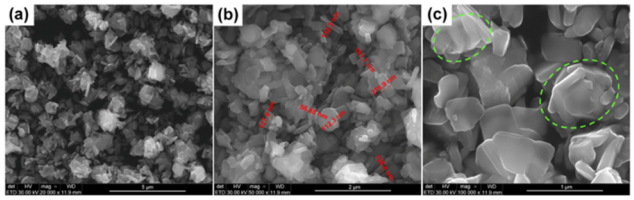

Fig. 2 FE-SEM images for **P** at different magnifications: (a) overall view (×20 000) and (b and c) details (×100 000 and ×200 000, respectively).

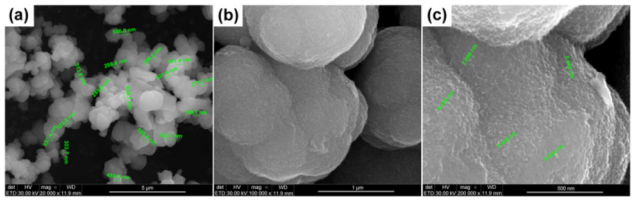

Fig. 3 FE-SEM images for sample **1** at different magnifications: (a) overall view (×20 000) and (b and c) details (×50 000 and ×100 000, respectively): green dashed ellipses in (c) indicate conglomerates formed by the self-assembly phenomena of elongated particles.

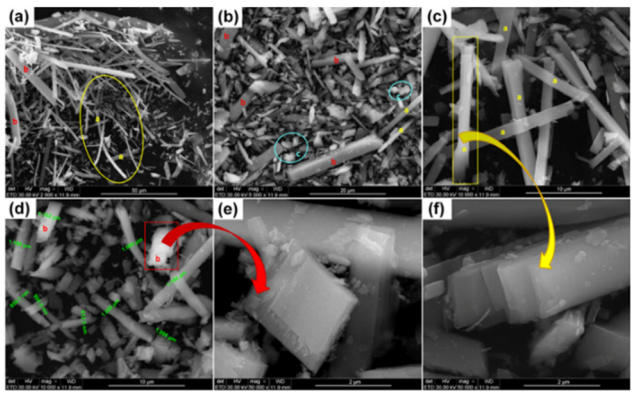

Fig. 4 FE-SEM images for **2** at different magnifications: (a and b) overall views (×2000 and ×5000): the letter "a" denotes belts and rods, while the solid yellow ellipse of (a) delimits an area where rods bundles are found; the letter "b" denotes thick prismatic aggregates; the letter "c" and solid light blue ellipses indicate submicron polyhedral particles; (c and d) higher-magnification images showing that the rod (yellow rectangle of (c)) and the prism (red rectangle of (d)) are actually hierarchical structures, and (e and f) details (×50 000) highlighting the mechanisms of the self-assembly phenomena.

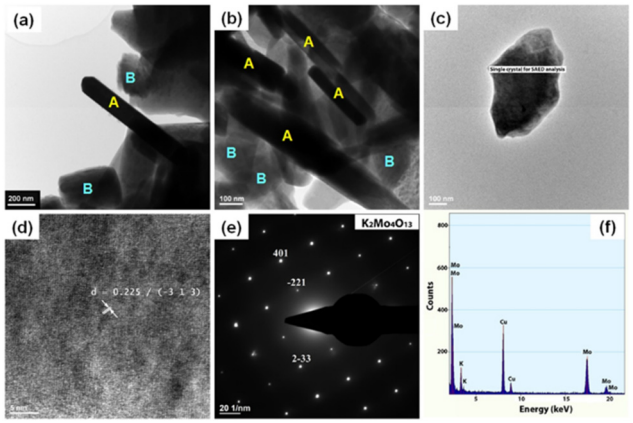

Fig. 5 (a and b) Bright-field global TEM images of different magnifications for **1** (400 °C): (A) α-MoO_3 and (B) $K_2Mo_4O_{13}$ crystals, (c) bright-field detailed TEM image of a $K_2Mo_4O_{13}$ single crystal, and (d) HR-TEM image, (e) SAED pattern and (f) EDX spectrum recorded on the single crystal depicted in (c).

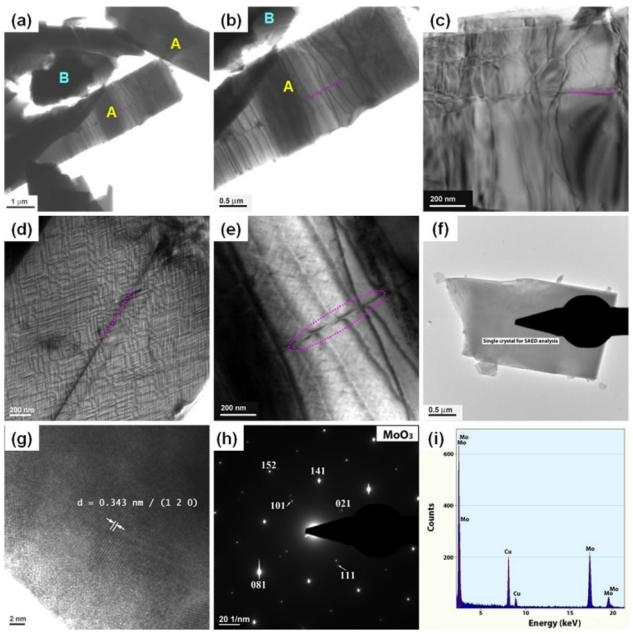

Fig. 6 (a and b) Bright-field global TEM images at different magnifications for **2** (500 °C): (A) MoO_3 and (B) $K_2Mo_4O_{13}$ crystals; (c and d) bright-field detailed TEM images and (e) dark-field detailed TEM image showing 1D hierarchical α-MoO_3 structures obtained by the self-assembly phenomena; (f) bright-field detailed TEM image of a MoO_3 single crystal; and (g) HR-TEM image, (h) SAED pattern and (i) EDX spectrum recorded on the single crystal depicted in (f).

very small equiaxial nanoparticles (up to 10 nm) well welded together (Fig. 2(b) and (c)). The qualitative EDX analysis (Fig. S12(e) in the ESI†) performed on the area presented in the FE-SEM image of Fig. S12(a) in the ESI† indicates the presence only of Mo, K and O elements. An almost homogeneous distribution of the cation species, showing the formation of hydrated K/MoO_x phases, is highlighted by the related elemental (Fig. S12(b) and (c) in the ESI†) and superimposed maps (Fig. S12(d) in the ESI†).

The FE-SEM images of **1** show the formation of almost evenly sized conglomerates of 1–1.5 μm, consisting of radially fused rod-like particles as well as of weakly faceted quasi-prismatic particles with rounded edges and corners (Fig. 3(a) and (b)). The length of these elongated particles varies between 50 nm and 150 nm (rods), and 200 up to 500 nm (quasi-prismatic particles). Equiaxial polyhedral particles sized in the

submicron and even nanometer range, most likely related to the secondary $K_2Mo_4O_{13}$ phase, were also noticed (Fig. 3(b)). The detailed view from the higher magnification FE-SEM image shows a tendency of the elongated particles to form conglomerates, both by welding together to create chemically homogeneous, fused bundles and by attaching at the surface of the polyhedral $K_2Mo_4O_{13}$ particles to create composite aggregates (green dashed ellipses in Fig. 3(c)).

The global EDX spectrum on a selected area indicated by the SEM image of **1** in Fig. S13(a) in the ESI† shows the presence of K, Mo and O elements (Fig. S13(b) in the ESI†), while in the EDX spectrum collected on a rod-like particle (Fig. S13(c) in the ESI†), only Mo and O were identified, proving that the elongated morphology is specific to the α-MoO_3 phase (Fig. S13(d) in the ESI†). The elemental mapping reveals that the chemical homogeneity is lower compared to that of **P** (Fig. S14(a) in the ESI†). However, a clear distinction of the two phases is not clearly highlighted (Fig. S14(b)–(e) in the ESI†). This observation agrees with a previous study regarding the thermal transformation process at 300–400 °C from the $NaNH_4Mo_3O_{10}{\cdot}H_2O$ single crystals to the hybrid material $Na_2Mo_4O_{13}$/α-MoO_3.[21]

For **2**, the lower-magnification FE-SEM images (Fig. 4(a) and (b)) display well-defined crystals of dissimilar morphologies: (i) rods and belt-like particles (width of 0.6–2 μm and variable length of 13–65 μm); (ii) thick 1D prismatic aggregates (side of the base of 3–8 μm and length of 30–70 μm) and (iii) submicron polyhedral particles. The higher magnification images show that the elongated 1D particles are hierarchical structures formed by the self-assembly phenomena (Fig. 4(c) and (d)). Some thin square-/rhombic lamellar crystals grow by lateral attaching into thin, rectangular ribbons, and are then stacked by overlapping, forming thick square prism-shaped aggregates (Fig. 4(e)) and long micro-rods/belts, respectively (Fig. 4(f)).

The thermally induced morphological changes in **2** are also accompanied by an obvious chemical heterogeneity. Thus, the elemental and superimposed EDX maps obtained on the area displayed in the BSE-SEM image (Fig. S15(a) in the ESI†) reveal the presence of Mo-rich regions corresponding to the 1D hierarchical structures of the α-MoO_3 phase, which coexist with K-rich aggregates of small, isotropic particles, associated with the secondary $K_2Mo_4O_{13}$ phase (Fig. S15(b)–(e) in the ESI†). The EDX spectrum confirms the presence of the Mo, K and O species identified by their specific peaks (Fig. S15(f) in the ESI†).

More insights into the morphological features of **1** and **2** were provided by performing TEM and HR-TEM investigations. For **1**, the TEM images of different magnifications displayed in Fig. 5(a) and (b) show a duplex-type morphology, suggesting the presence of a mixture of two crystalline phases, in agreement with the XRD findings. Thereby, well-defined, rod-like structures, denoted as "A", of a width of 75–170 nm and a variable length of 200–600 nm, co-exist with unevenly shaped and sized polyhedral particles, denoted as "B". Considering the above results of the SEM-EDX investigations (Fig. 3–5) and other literature data,[9–16] the 1D structures correspond to the major crystalline α-MoO_3 phase.

HR-TEM and SAED investigations performed on the isolated particle with a size of *ca.* 550 nm, displayed in Fig. 5(c), proved that the equiaxially polyhedral morphology corresponds to the secondary $K_2Mo_4O_{13}$ phase. Indeed, the long-range ordered fringes, assigned to the crystalline plane (−3 1 3) in the HR-TEM image (Fig. 5(d)), as well as the ordered bright spots (which proves the single-crystal nature of the particle), indexed as the crystalline planes (2 −3 3), (−2 2 1) and (4 0 1) in the SAED pattern (Fig. 5(e)), are specific to the triclinic structure of the $K_2Mo_4O_{13}$ compound. The global EDX spectrum (Fig. 5(f)) collected on the area shown in the TEM image (Fig. 5(c)) reveals the presence of all elemental species (Mo, K and O) belonging to the $K_2Mo_4O_{13}$ phase in **1**. The reports regarding potassium tetramolybdate are rare, especially concerning its morphology.[51,52] To date, only two examples of $K_2Mo_4O_{13}$ with a nanobelt-type morphology have been investigated.[51,52] Therefore, the clear separation between the two crystalline phases in **2**, discussed below, provided us the opportunity for a rare morphological study of $K_2Mo_4O_{13}$.

TEM investigation of **2** points out the presence of the two phases, *i.e.* α-MoO_3 and $K_2Mo_4O_{13}$, as the images of different magnifications reveal (Fig. 6(a) and (b)). A focus on a single 1D micro-belt suggests a stepped assembly process. The first stage involves a layer-by-layer [001] growth determined by the vertical assembly of a large number of thin foils to form a rod-like 1D structure, while in the second step, a longitudinal fusion of two rods along the [010] crystallographic axis leads to the formation of a belt-like architecture with a width of ~2 μm (Fig. 6(b) and (c)). The hierarchization level can be even higher due to more complex self-assembly mechanisms (see Scheme 1) involving cross-joining of nanocrystallites within the rods (Fig. 6(d)), followed by longitudinal coalescence of several rods inside a bundle, in order to form 1D micro-belts (Fig. 6(c) and (d)) and, finally, a further growth through an end-to-end fusion (marked by the dotted magenta ellipse, Fig. 6(e)) of several such micro-belt-shaped conglomerates to create lengthwise extended 1D hierarchical aggregates (Fig. 6(e)).

Scheme 1 depicts the very complex self-assembly mechanism for **2** that led to different hierarchically structured 1-D morphologies of α-MoO_3:

- Ribbon-like particles resulted through the longitudinal attachment of slab crystals along the [010] direction (green rectangle) that are further stacked and/or are fused.

- Belt-like and rod particles which grow further into thick prisms and extended prisms.

The HR-TEM and SAED analyses on the thin, lamellar single crystal of Fig. 6(f) revealed the crystalline planes specific to the orthorhombic structure of α-MoO_3 (Fig. 6(g) and (h)), while the lack of the K-bearing species in the EDX spectrum undoubtedly highlighted that this kind of morphology is related to the MoO_3 phase (Fig. 6(i)). It is interesting to note how the structural anisotropy of the unit cell of MoO_3 (Table 1) is also preserved at the morphological level by the formation of both rod-/belt-like crystals and 1D hierarchical aggregates.

Although all these 1D morphology types were identified, the overview SEM images (Fig. 4a) confirm the prevalence of

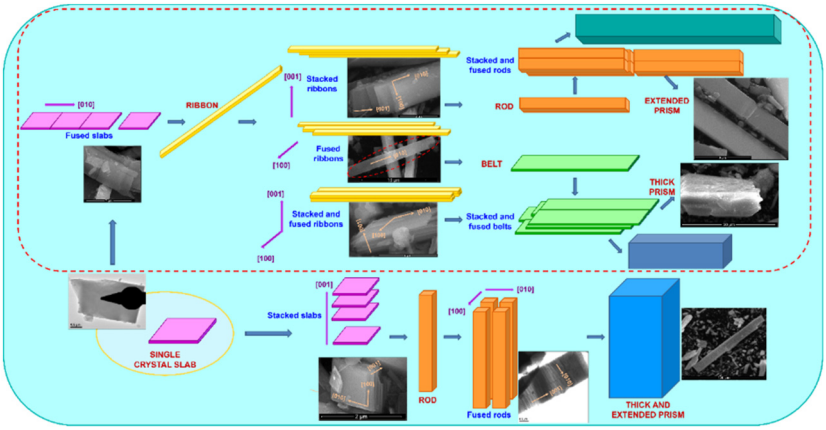

Scheme 1 The schematic representation of the complex self-assembly mechanism of different 1-D morphologies of the α-MoO_3 crystalline component in **2**.

rods grown along the [010] preferential direction. It is also important to note that as the temperature increases from 400 (**1**) to 500 °C (**2**), a longitudinal fusion of several rods along the crystallographic [010] axis became even more significant, leading to the formation of belt-like morphologies, which continues to grow through an end-to-end fusion to create lengthwise extended 1D hierarchical aggregates. These observations are consistent with the XRD results. Thus, for **1**, the intensity of the (002) reflection from $2\theta = 49.26°$ is lower than the intensity of the (020) reflection from $2\theta = 12.77°$, so that the $I(020)/I(002)$ ratio is 4.55, much higher than that calculated from ICDD file no. 01-086-8446 ($I(020)/I(002) = 1.61$). This indicates a higher frequency in the occurrence of crystalline planes ($0k0$) compared to planes ($00l$). For **2**, the value of this ratio is doubled, *i.e.* $I(020)/I(002) = 9.15$, relative to that corresponding to **1**. Correlation of the Rietveld analysis of the XRD data with TEM results suggests that at 400 °C, the self-assembly process of the crystals into 1D structures in α-MoO_3 is just at the beginning. The increase of the calcining temperature to 500° C promotes the self-assembly phenomena of foils, involving the development of more and more complicated hierarchical 1D architectures.

Electrochemical properties of P, 1 and 2 materials

Due to multiple oxidation states of molybdenum, the hydrated K/MoO_x (**P**) and α-MoO_3–$K_2Mo_4O_{13}$ crystalline mixtures (**1** and **2**), one may presume that these materials might have a good capacitive performance. This assumption is also supported by other reports which attested that the layered structure of α-MoO_3 with 1-D morphologies proved to be suitable in supercapacitor applications.[13–16]

The capacitive features of **P/G**, **1/G** and **2/G** electrode-modified materials were extensively investigated through cyclic voltammetry (CV) and galvanostatic charge–discharge (GCD) tests, in three-electrode setup experiments, using an aqueous solution of 0.5 M Na_2SO_4 as the electrolyte.

The CV plots for **P/G**, **1/G** and **2/G** were recorded between −0.6 and 0 V at different sweep rates varying from 5 up to 200 mV s^{-1}. The overlapped CV plots selected at a sweep rate of 20 mV s^{-1} are presented in Fig. 7a. Also, the superimposed CV curves of **2/G** recorded at sweep rates ranging from 5 to 200 mV s^{-1} are presented in Fig. S16a in the ESI.†

In all three cases, the CV curves exhibit almost a quasi-rectangular shape (Fig. 7a), most likely due to the fact that the charge is mainly accumulated through the electrochemical double layer where no significant faradaic processes are observed.[53] These findings are not surprising because a similar behavior was also observed for other MoO_3-based electrodes.[53] Fig. 7a appears to indicate an increase of electrochemical performance from the graphite electrode (**G**) modified with the **P** amorphous material (**P/G**) up to **G** modified with **1** (**1/G**) and **2** (**2/G**), respectively, crystalline hybrid materials. The gravimetric capacitance[54] was estimated through the following eqn (1):

$$C = Q/(2 \times m \times (V_a - V_c)), \quad (1)$$

where C is the areal capacitance, Q is the electric charge integrated over the entire curve, m is the mass of the electroactive material and $V_a - V_c$ is the potential range within which the potential was scanned.

At a sweep rate of 20 mV s^{-1} for **P/G**, **1/G** and **2/G**, the resulting values are 0.54 F g^{-1}, 4.25 F g^{-1}, and 12.65 F g^{-1}, respectively, pointing out that **1/G**- and **2/G**-modified electrodes exhibit better capacitive performances than **P/G**-modified electrodes. These results are supported by those estimated from the CVs recorded at different sweep rates from 5 mV s^{-1} to 200 mV s^{-1} (Fig. 7b), which revealed that **2/G** shows the highest values of C, whereas **P/G** shows the lowest one, regardless of the sweep rate. The maximum value of C, 20.45 F g^{-1}, is attained for the **2/G**-modified electrode at a sweep rate of 5 mV s^{-1}. Under our experimental conditions, the modified electrodes with amorphous K/MoO_x hydrated material (**P/G**) as well as with the crystalline mixture α-MoO_3/$K_2Mo_4O_{13}$ (**1/G** and **2/G**) acted as cathodes in the electrochemical process. A similar behavior was also observed for other modified electrodes with

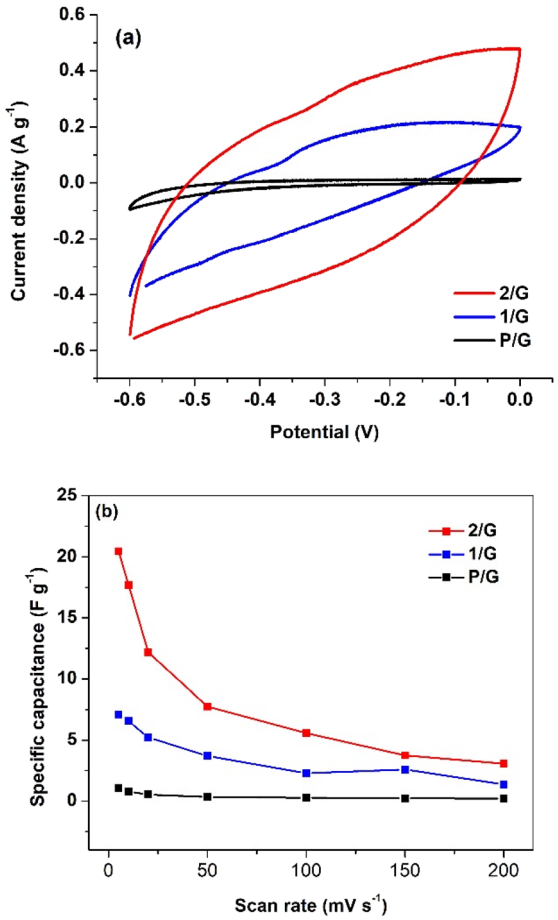

Fig. 7 (a) Overlapped CV plots for **P/G**, **1/G** and **2/G** modified electrodes recorded at a 20 mV s^{-1} sweep rate. (b) The variation of gravimetric capacitance values, *C*, of **P/G**, **1/G** and **2/G** modified electrodes with the sweep rate, *v*, using 0.5 M aqueous solution of Na_2SO_4 as the electrolyte (the lines are guides for the eye).

Mo-based oxide/composite materials such as for the nanostructured/nanobelts of α-MoO_3 oxides in 0.005 M H_2SO_4/0.095 M Na_2SO_4,[55] or in 0.5 M Li_2SO_4,[56] and for MoO_3–ZnO composites using 1 M Na_2SO_4 electrolyte[57] or for K^+ pre-intercalated hydrogenated MoO_3 (K_yMoO_{3-x}) materials.[58]

The GCD tests were carried out on **P/G**, **1/G** and **2/G** at different current densities and the relevant results are shown in Fig. 8 and Fig. S17 in the ESI.† It appears that these electrodes are charging and discharging linearly and symmetrically, suggesting that the electrical charge likely accumulates physically, mainly through a non-faradaic mechanism with a typical EDCL behaviour.[59,60] These findings are in good agreement with those observed from CV investigations.

The gravimetric capacitances were estimated from the charge–discharge curves[61] through eqn (2):

$$C = (I \times \Delta t)/(\Delta V \times m), \quad (2)$$

where *C* is the specific capacitance, *I* is the current (A), Δt is the discharging time (s), ΔV is the potential window (V), and *m* is the mass of the electroactive material (g).

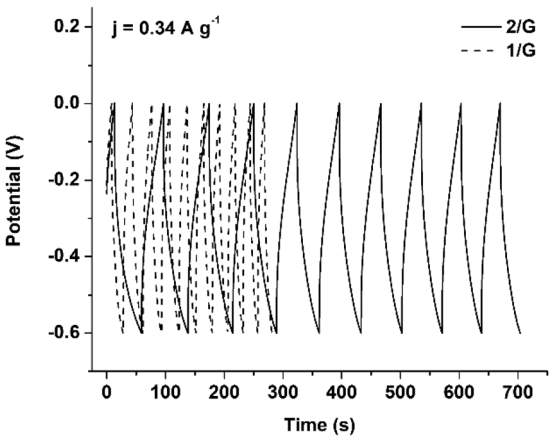

Fig. 8 GCD curves of **2/G** and **1/G** at an applied current density of 0.34 A g^{-1} in 0.5 M Na_2SO_4.

The resulting *C* values are *ca.* 2.5 times higher at **2/G** (*i.e. ca.* 22.24 F g^{-1}) compared to **1/G** (*i.e. ca.* 8.33 F g^{-1}) at an applied current density of 0.34 A g^{-1}, revealing that the graphite substrate covered with well-separated α-MoO_3–$K_2Mo_4O_{13}$ crystalline phases (**2/G**) exhibits the best charge storage capability. Conversely, **P/G** shows a very low gravimetric capacitance (*i.e.* 0.76 F g^{-1} at an applied current density of 0.07 A g^{-1}), suggesting a poor capacitive performance. These results certify previous ones from CV investigations. From the charge–discharge curves of these types of electrodes, no sudden drop of the potential might be observed during the initial discharge, demonstrating that all three types of electrodes have low internal resistance.

Improved electrochemical performances could be obtained by modifying the graphite electrode with the best electrochemically responsive material of the series, **2**, physically mixed with graphene. The added graphene is expected to increase the conductivity of the material and, also, to prevent the agglomeration of the particles of **2**. The capacitive performance of these new assembled electrodes denoted as **2-Gr/G** was assessed. For comparison, the electrochemical investigations were carried out at the graphene-modified graphite electrode denoted as **Gr/G**. As in the case of **2/G**, the CV plot of **2-Gr/G** exhibits a quasi-rectangular shape (Fig. 9), suggesting that the presence of graphene does not change the type of charging of these Mo-based electrodes. In other words, at these **2-Gr/G** electrodes, the charge storage capacity also originates mainly through the electric double layer charge as evidenced for other MoO_3-based electrodes in Na_2SO_4.[53]

These findings are also supported by the CV plots recorded for **2/G** (Fig. S16a in the ESI†) and **2-Gr/G** (Fig. S16b in the ESI†) at different sweep rates ranging from 5 mV s^{-1} up to 200 mV s^{-1}. The gravimetric capacitance of **2-Gr/G** estimated from the CVs recorded at 20 mV s^{-1} is 26.46 F g^{-1}, which is *ca.* 2.6 times higher than that of **Gr/G** (*i.e.* 10 F g^{-1}) and *ca.* two times higher than that of the **2/G** electrode (*i.e.* 12.65 F g^{-1}).

The GCD curves were recorded for **2-Gr/G** at several current densities. A comparison of the GCD curves for **2-Gr/G** and **2/G**

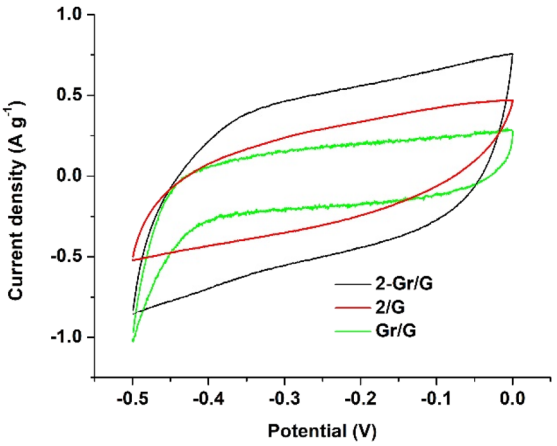

Fig. 9 CVs of **2-Gr/G**, **2/G** and **Gr/G** at 20 mV s^{-1} in 0.5 M aqueous solution of Na_2SO_4.

recorded at a current density of 1 A g^{-1} is presented in Fig. 10a and illustrates the superior capacity storage of the graphene-added electrode **2-Gr/G**. From the charge–discharge curves of both **2-Gr/G** and **2/G** recorded at several current densities, the corresponding gravimetric capacitances were estimated (Fig. 10b). The gravimetric capacitances of **2-Gr/G** are 33.21 F g^{-1}, 32.91 F g^{-1}, 102.31 F g^{-1} and 145 F g^{-1} at the applied current densities of 1 A g^{-1}, 0.64 A g^{-1}, 0.34 A g^{-1} and 0.166 A g^{-1}, respectively, whereas the corresponding results for **2/G** are 7.91 F g^{-1}, 13.35 F g^{-1}, 22.24 F g^{-1} and 32.98 F g^{-1}. These results, which are in good agreement with those from CV investigations, point out clearly that the graphite modified with the mixture **2-Gr** enables higher gravimetric capacitance (*i.e.* four times higher) compared to that observed in the absence of graphene, regardless of the applied current densities. SEM investigations were carried out on bare graphite (**G**) and **2/G**- and **2-Gr/G**-modified electrodes (Fig. S18 in the ESI†) and one can clearly observe that **2/G** and **2-Gr/G** are well covered with **2**, mostly showing 1-D morphologies. Moreover, by mixing **2** with graphene (**2-Gr**), the particles are more dispersed on the graphite substrate. Graphene seems to prevent to a certain extent the agglomeration of Mo-based particles.[62] In this way, the diffusion of the electrolyte ions to the electrode surface is facilitated, leading to an improved charge-storage capability for the **2-Gr/G**-modified electrode.

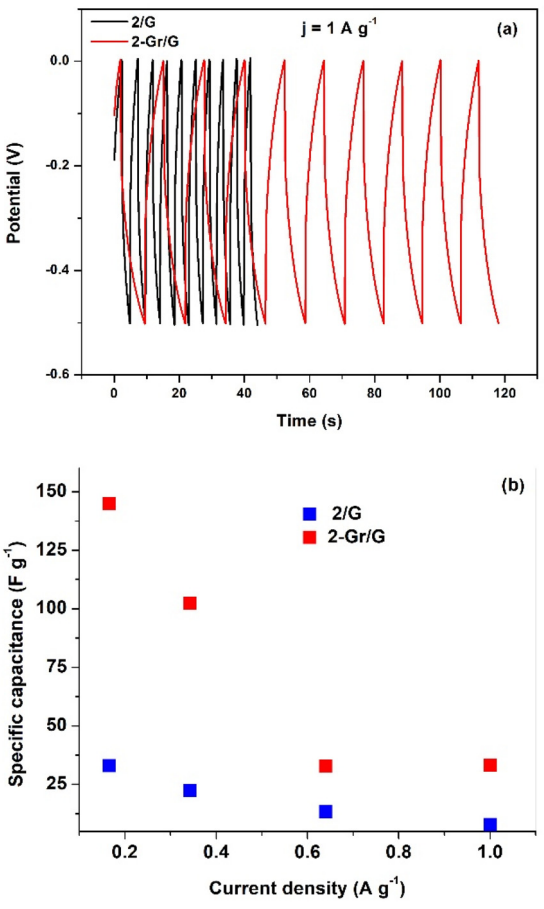

Fig. 10 (a) Overlapped GCD curves of **2-G** and **2-Gr/G** at an applied current density of 1 A g^{-1} in 0.5 M aqueous solution of Na_2SO_4 (*j* is the current density). (b) Gravimetric capacitances at various current densities for **2-G** and **2-Gr/G** in 0.5 M aqueous solution of Na_2SO_4.

These results are close to those obtained for other MoO_3-based electrodes, the charge storage capability of our material being similar.[63–65] For instance, a specific capacitance of 176 F g^{-1} for an applied current density of 0.001 A g^{-1} was found for α-MoO_3 mixed with carbon black,[63] a value of 80.7 F g^{-1} for an applied current density of 0.2 A g^{-1} was estimated for β-MoO_3 coated with carbon,[64] and for the *h*-MoO_3-based electrodes, for an applied current density of 0.2 A g^{-1}, a specific capacitance of 229 F g^{-1} was determined.[65]

Additional information about the electrochemical features of the α-MoO_3–$K_2Mo_4O_{13}$-based electrodes were attained from EIS investigations carried out in 0.5 M aqueous solution of Na_2SO_4 as an electrolyte at open circuit. The Nyquist plots of **1/G**, **2/G** and **2-Gr/G** as well as the electrical equivalent circuit[60,61,66,67] used for fitting the corresponding impedance spectra are shown in Fig. 11. The estimated R_s, which represents the electrolyte resistance combined with the electrical wire resistance and internal resistance of electrodes, is low regardless of the type of electrode (*i.e.* 3.48, 6.77 and 3.49 ohm cm^2 for **1/G**, **2/G** and **2-Gr/G**, respectively), suggesting that the electrodes have low internal resistance.[59] The leakage resistance R_L is high for all types of electrodes, *i.e.* **1/G**, **2/G** and **2-Gr/G**, attesting that, at these samples, low leakage current occurs. These features (low R_s and high R_L) are of great importance in obtaining electrodes with good capacitive behaviour.[55,58] The R_{ct}, which accounts for interfacial charge transfer resistance, is much lower at **2/G** (*i.e.* 29.85 ohm cm^2) compared to **1/G** (*i.e.* 519.9 ohm cm^2), suggesting that the electrode **2/G** has a higher conductivity.[60] The Warburg resistance (W), which is a type of impedance associated with diffusion processes, is much lower for **2** (*i.e.* 660 ohm cm^2) compared to **1** (6489 ohm cm^2), confirming that **2/G** allows better ion diffusion.[55,59] The values estimated for CPE_{DL}, which might be roughly associated with double layer capacitance, are quite

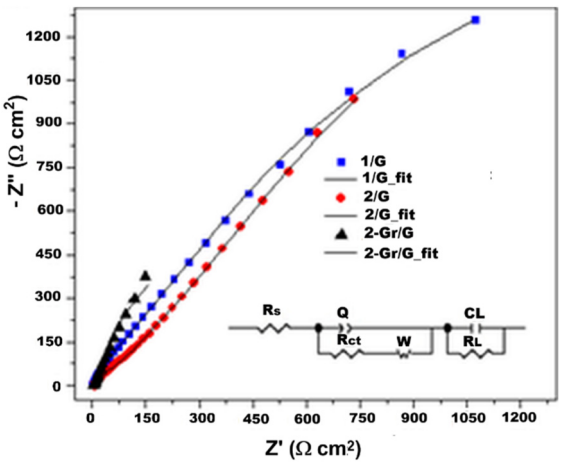

Fig. 11 Nyquist plots of **1/G**, **2/G** and **2-Gr/G** and their simulated curves (solid lines). The inset shows the electrical equivalent circuit used to simulate the impedance spectra. The equivalent considers the solution resistance R_s, the charge transfer characteristics R_{ct}, the constant phase element of the double layer Q, the Warburg element W, and the leakage resistance R_L associated in parallel with CL.

similar for both types of electrodes (*i.e.* 0.003 ohm^{-1} cm^{-2} s^n for **1/G** and 0.002 ohm^{-1} cm^{-2} s^n for **2/G**), indicating that a good contact area at the electrode–electrolyte surface is achieved in both cases. Also, the more efficient charge-storage capacity of the **2/G**-modified electrode compared to **1/G** might be linked to its higher conductivity and good contact area at the electrode–electrolyte interface and to a lower diffusion path resistance (W). After modifying the graphite substrate with the mixture of graphene and **2**, the R_{ct} and W significantly decrease (R_{ct} and W are 2.03 ohm cm^2 and 34 ohm cm^2, respectively, for **2-Gr/G**), while the CPE_{DL} increases (0.009 ohm^{-1} cm^{-2} s^n for **2-Gr/G**). The presence of graphene enhances the conductivity of the electrode material, increases the contact area at the electrode electrolyte interface and promotes the diffusion of the electrolyte ions to the electrode surface, thus improving the charge-storage capability of these **2-Gr/G**-modified electrodes.

We can conclude that the new Mo-based hybrid materials exhibit good capacitive properties, as indicated by CV and GCD. The composition and morphostructural features of **P**, **1** and **2** hybrid materials play key roles in their electrochemical performance. Thus, the compact aggregation of nanoparticles of the amorphous K/MoO_x (**P**, see Fig. 3) lacks efficient accessibility of the electrolyte ions to the **P/G**-modified electrode surface, resulting in most probably low C values. Furthermore, the co-existence of two crystalline phases, α-MoO_3 and $K_2Mo_4O_{13}$, clearly improved the capacitive properties for **1** and **2** materials. Nevertheless, the well-defined and separated 1-D microstructures of α-MoO_3 and polyhedral particles of $K_2Mo_4O_{13}$ (see Fig. 4) from the **2/G**-modified electrode provide the best capacitive properties.

Results thus far indicate that the morphology of K/Mo hybrid structures plays a pivotal role in their capacitive properties. Therefore, it appears that different morphologies have a great impact on the surface area, ion diffusion pathways, electrical conductivity, and structural stability, all of which are critical for optimal capacitive performance. Thus, one-dimensional structures of the major component of **2**, α-MoO_3, provide direct pathways for electron transport and ion diffusion, leading to enhanced specific capacitance and rate capability.[68] Moreover, the presence of the sub-micron polyhedral particles of t-$K_2Mo_4O_{13}$, the co-existent crystalline phase from **2**, offers a high surface area and facilitates electrolyte penetration, improving charge storage capacity.[69] It is also worth noting that the existence of the 1-D hierarchical structures of α-MoO_3 in **2** (see Scheme 1) demonstrated by the HR-TEM investigation might help mitigate volume expansion/contraction during cycling, thus improving long-term stability.[70] The trend is also preserved for the **2-Gr/G**-modified electrode with the mention that the charge storage capacity is even more enhanced due to the synergistic action of graphene and **2**, and also due to the well-dispersed particles of **2** within the graphene substrate which increases the electrode–electrolyte contact area.

Conclusions

New K/Mo-based hybrid materials were obtained through the hydrothermal method and post-synthesis calcination treatments using, for the first time, the potassium octacyanomolybdate(IV) complex as a single molecular precursor: hydrated K/MoO_x amorphous phase, **P**, and its calcination products at 400 (**1**) and 500 °C (**2**), respectively, both comprising a rare combination of the orthorhombic α-MoO_3 and triclinic $K_2Mo_4O_{13}$ crystalline phases, in close percentages. Thermal treatment strongly influences the particles sizes and morphology of the K/Mo-based materials: (i) compact micro-spherical aggregates of different dimensions (275–750 nm) of equiaxial nano-sized particles of **P** (5–9 nm), with K and Mo elements uniformly distributed throughout the sample; (ii) large conglomerates (1–1.5 μm) of fused rods/prisms of α-MoO_3 and polyhedral particles of $K_2Mo_4O_{13}$ in **1** and (iii) in **2**, well-separated microparticles of α-MoO_3 with 1-D morphology (rods, belts and thick prisms) and sub-micron polyhedral particles of potassium tetramolybdate. It is worth noting that in **2**, the different hierarchically structured 1-D morphologies of molybdenum oxide resulted through a complex self-assembly mechanism and, moreover, the separated $K_2Mo_4O_{13}$ crystalline phase offered the opportunity for a unique morphological study. The capacitive properties of **P**-, **1**- and **2**-modified graphite electrodes were investigated, showing a predominant EDCL behaviour as well the key roles played by the morphology of the K/Mo hybrid materials. The best capacitor performances were achieved for the **2/G**-modified electrode likely due to the co-existence of well-separated microbelts of α-MoO_3 and polyhedral $K_2Mo_4O_{13}$ particles that provides a large electrode–electrolyte contact surface area. Moreover, the combined capacitive features of **2** with the high conductivity/high surface area of

carbonaceous support like graphene led to four times higher gravimetric capacitance of the **2-Gr/G**-modified electrode.

Our results open large perspectives in a less explored area of cyano-based complexes of the late row metals as single-source precursors of 4d/5d nano- and micro-sized oxide materials. Besides, the hydro-/solvothermal synthesis is a scalable method that provides high flexibility with regard to the reaction parameters and starting complexes that will allow us to modulate the composition as well as to tailor the morphostructural features of the Mo-based oxides for the design of new generation of highly efficient capacitors.

Conflicts of interest

There are no conflicts to declare.

Data availability

The authors of the submitted manuscript entitled *Rare α-MoO_3–$K_2Mo_4O_{13}$ hybrid structures obtained via a single molecular precursor approach* declare that the data supporting this article have been included as part of the ESI.†

Acknowledgements

This work was supported by a grant of the Romanian Ministry of Education and Research, CNCS – UEFISCDI, project number PN-III-P4-ID-PCE-2020-2324, within PNCDI III. Also, this work was carried out within the research plan of the Institute of Physical Chemistry – Ilie Murgulescu, themes Electrochemical preparation and characterization of active materials with predetermined features and Green synthesis of materials. The authors are grateful to the Ministry of Research, Development and Innovation through the National Program "Installations and Strategic Objectives of National Interest" for access to the infrastructure.

References

1 H. Ren, S. Sun, J. Cui and X. Li, *Cryst. Growth Des.*, 2018, **18**, 6326.
2 H. Y. Gehara and H. Yamashita, *Chem. Commun.*, 2022, **58**, 8466.
3 A. V. Avani and E. I. Anila, *Int. J. Hydrogen Energy*, 2022, **47**, 20475.
4 M. Ranjbar, F. Delalat and H. Salamati, *Appl. Surf. Sci.*, 2017, **396**, 1752.
5 T. A. Tran, K. Krishnamoorthy, Y. W. Song, S. K. Cho and S. J. Kim, *ACS Appl. Mater. Interfaces*, 2014, **6**, 2980.
6 S. Pandey, K. H. Sharma, A. K. Sharma, Y. Nerthigan, D.-R. Hang and H.-F. Wu, *Chem. – Eur. J.*, 2018, **24**, 7417.
7 A. Hermawan, N. L. W. Septiani, A. Taufik, B. Yuliarto and S. Y. Suyatman, *Nano-Micro Lett.*, 2021, **13**, 207.
8 I. A. de Castro, R. S. Datta, J. Z. Ou, A. Castellanos-Gomez, S. Sriram, T. Daeneke and K. Kalantar-zadeh, *Adv. Mater.*, 2017, **29**, 1701619.
9 X. He, H. Zhang, X. Zhao, P. Zhang, M. Chen, Z. Zheng, Z. Han, T. Zhu, Y. Tong and X. Lu, *Adv. Sci.*, 2019, **6**, 1900151.
10 L. Mai, F. Yang, Y. Zhao, X. Xu, L. Xu, B. Hu, Y. Luo and H. Liu, *Mater. Today*, 2011, **14**, 346.
11 R.-Q. Song, A.-W. Xu, B. Deng and Y.-P. Fang, *J. Phys. Chem. B*, 2005, **109**, 22758.
12 R. Malik, N. Vijay and K. Tomer, *Mater. Adv.*, 2021, **2**, 4190.
13 K. Tang, S. A. Farooqi, X. Wang and C. Yan, *ChemSusChem*, 2019, **12**, 755.
14 N. Maheswari and G. Muralidharan, *Appl. Surf. Sci.*, 2017, **416**, 461.
15 S. D. Raut, N. M. Shinde, B. G. Ghule, S. Kim, J. J. Pak, Q. Xia and R. S. Mane, *Chem. Eng. J.*, 2022, **433**, 133627.
16 C. V. Raman, A. Mauger and C. M. Julien, *Prog. Cryst. Growth Charact.*, 2021, **67**, 100533.
17 Z. Zhang, Y. Gao and Q. Wang, *Sep. Purif. Technol.*, 2018, **19**, 354.
18 Y. Zhang, Z. Zhang, Q. Yan and Q. Wang, *Appl. Catal., A*, 2016, **511**, 47.
19 M. Hu, H. Jing, T. Li, J. Wang, H. Yang, R. Lv and D. Chen, *J. Mater. Chem. A*, 2019, **7**, 10954.
20 N. Sotani, T. Suzuki and K. Eda, *J. Solid State Chem.*, 1997, **132**, 330.
21 Z. Zhang, R. Yang, Y. Gao, Y. Zhao, J. Wang, L. Huang, J. Guo, T. Zhou, P. Lu, Z. Guo and Q. Wang, *Sci. Rep.*, 2014, **4**, 6797.
22 J. Chen, L. Wei, A. Mahmood, Z. Pei, Z. Zhou, X. Chen and Y. Chen, *Energy Storage Mater.*, 2020, **25**, 585.
23 M. Cao, T. Liu, S. Gao, G. Sun, X. Wu, C. Hu and Z. L. Wang, *Angew. Chem., Int. Ed.*, 2005, **44**, 4197.
24 M. Hu, J.-S. Jiang and X. Li, *Cryst. Growth Des.*, 2009, **9**, 820.
25 P. Du, L. X. Song, J. Xia, Y. Teng and Z. K. Yang, *J. Mater. Chem. A*, 2014, **2**, 11439.
26 S. Bharathi, D. Nataraj, M. Seetha, D. Mangalaraj, N. Ponpandian, Y. Masuda, K. Senthile and K. Yong, *CrystEngComm*, 2010, **12**, 373.
27 Y. Chen, Y. Wang, X. Shen, R. Cai, H. Yang, K. Xu, A. Yuan and Z. Ji, *J. Mater. Chem. A*, 2018, **6**, 1048.
28 Y. Chen, W. Zong, H. Chen, Z. Li, H. Pang, A. Yuan, H. Yang and X. Shen, *Chem. Eng. J.*, 2021, **426**, 130347.
29 S. Chorazy, J. Zakrzewski, M. Magott, T. Korzeniak, B. Nowicka, D. Pinkowicz, R. Podgajny and B. Sieklucka, *Chem. Soc. Rev.*, 2020, **49**, 5945.
30 D. Kwak, M. Wang, K. J. Koski, L. Zhang, H. Sokol, R. Maric and Y. Lei, *ACS Appl. Mater. Interfaces*, 2019, **11**, 10697.
31 L. Zhou, L. Yang, P. Yuan, J. Zou, Y. Wu and C. Yu, *J. Phys. Chem. C*, 2010, **114**, 21868.
32 X. W. Lou and H. C. Zeng, *Chem. Mater.*, 2002, **14**, 4781.
33 J. G. Leipoldt, L. D. C. Bok and P. J. Cilliers, *Z. Anorg. Allg. Chem.*, 1974, **409**, 343.
34 T. Xia, Q. Li, X. Liu, J. Meng and X. Cao, *J. Phys. Chem. B*, 2006, **110**, 2006.

35 S. P. Goel, S. Kumar and M. P. Sharma, *Thermochim. Acta*, 1991, **188**, 201.
36 S. P. Goel, G. R. Verma and S. Kumar, *J. Anal. Appl. Pyrolysis.*, 1990, **18**, 91.
37 Q. Huang, S. Hu, J. Zhuang and X. Wang, *Chem. – Eur. J.*, 2012, **18**, 15283.
38 E. Ghaleghafi and M. B. Rahmani, *Solid State Sci.*, 2019, **94**, 85.
39 M. Kassem, *Res. Chem. Intermed.*, 2015, **41**, 2891.
40 K. Eda, K. Chin, N. Sotani and M. S. Whittingham, *J. Solid State Chem.*, 2004, **177**, 916.
41 A. Chithambararaj, N. R. Yogamalar and A. C. Bose, *Cryst. Growth Des.*, 2016, **16**, 1984.
42 W. A. Dollase, *J. Appl. Crystallogr.*, 1986, **19**, 267.
43 H. Sitepu, *Powder Diffr.*, 2009, **24**, 315.
44 L. Seguin, M. Figlarz, R. Cavagnat and J.-C. Lassègues, *Spectrochim. Acta, Part A*, 1995, **51**, 1323.
45 R. Nadimicherla, R. Zha, L. Wei and X. Guo, *J. Alloys Compd.*, 2016, **687**, 79.
46 S. Bai, S. Chen, L. Chen, K. Zhang, R. Luo, D. Li and C. C. Liu, *Sens. Actuators, B*, 2012, **174**, 51.
47 B. Gao, H. Fan and X. Zhang, *J. Phys. Chem. Solids*, 2012, **73**, 423.
48 Y. Sun, J. Wang, B. Zhao, R. Cai, R. Ran and Z. Shao, *J. Mater. Chem. A*, 2013, **1**, 4736.
49 K. Schofield, *Energy Fuels*, 2005, **19**, 1898.
50 Y. K. Voronko, A. A. Sobol and V. E. Shukshin, *Inorg. Mater.*, 2014, **50**, 844.
51 Z. Zhang, C. Hu, Y. Zhu, S. Xu, X. He, M. Hashim and D. Xiang, *Micro Nano Lett.*, 2011, **6**, 718.
52 L. Hernán and J. Morales, *Mater. Res. Bull.*, 1989, **94**, 1017.
53 P. Nagaraju, M. Arivanandhan, A. Alsalme, A. Alghamdib and R. Jayavel, *RSC Adv.*, 2020, **10**, 22836.
54 M. Qiu, P. Sun, L. Shen, K. Wang, S. Song, X. Yu, S. Tan, C. Zhao and W. Mai, *J. Mater. Chem. A*, 2016, **4**, 7266; H. Farsi, F. Global, H. Raissi and S. Moghiminia, *J. Solid State Electrochem.*, 2010, **14**, 643.
55 H. Farsi, F. Global, H. Raissi and S. Moghiminia, *J. Solid State Electrochem.*, 2010, **14**, 643.
56 J. Li and X. Liu, *CrystEngComm*, 2014, **16**, 184.
57 S. Muduli, S. K. Pati, S. Swain and S. K. Martha, *Energy Fuels*, 2021, **35**, 16850.
58 X. Xiao, C. J. Zhang, S. Lina, L. Huang, Z. Hu, Y. Cheng, T. Li, W. Qiao, D. Long, Y. Huang, L. Maid, Y. Gogotsi and J. Zhou, *Energy Storage Mater.*, 2015, **1**, 1.
59 M. Marcu, L. Preda, S. Vizireanu, B. Bita, M. A. Mihai, T. Spataru, T. Acsente, G. Dinescu and N. Spataru, *Mater. Sci. Eng., B*, 2022, **277**, 115585.
60 L. G. Coman, M. Marcu, T. Acsente, S. Vizireanu, V. Satulu, G. Dinescu, E. Matei, T. Spataru, N. Spataru and L. Preda, *Diamond Relat. Mater.*, 2023, **139**, 110316.
61 J. W. Lee, A. S. Hall, J. D. Kim and T. E. Mallouk, *Chem. Mater.*, 2012, **24**, 1158.
62 N. Spataru, J. M. Calderon-Moreno, P. Osiceanu, T. Kondo, C. Terashima, M. Popa, M. M. Radu, D. Culita, L. Preda, M. A. Mihai and T. Spataru, *Chem. Eng. J.*, 2020, **402**, 126258.
63 N. G. Prakash, M. Dhananjaya, A. Lakshmi Narayana, D. P. M. D. Shaik, P. Rosaiah and O. M. Hussain, *Ceram. Int.*, 2018, **44**, 9967.
64 A. V. Salkar, A. P. Naik, G. D. J. G. Pena, G. Bharath, M. A. Haija, F. Banat and P. P. Morajkar, *J. Energy Storage*, 2022, **48**, 103958.
65 Y. Niu, X. Li, H. Su, J. Li and Y. Qi, *Mater. Lett.*, 2022, **316**, 132062.
66 W. Wang, S. Guo, I. Lee, K. Ahmed, J. Zhong, Z. Favors, F. Zaera, M. Ozkan and C. S. Ozkan, *Sci. Rep.*, 2014, **4**, 4452.
67 X. Xiao, S. Li, H. Wei, D. Sun, Y. Wu, G. Jin, F. Wang and Y. Zou, *J. Mater. Sci.: Mater. Electron.*, 2015, **26**, 4226.
68 G. P. Nunna, D. Merum, T. J. Ko, J. Choi and M. H. Obili, *Int. J. Energy Res.*, 2022, **46**, 5973.
69 T. Brezesinski, J. Wang, S. Tolbert and B. Dunn, *Nat. Mater.*, 2010, **9**, 146.
70 J. Chen, S. Han, H. Zhao, J. Bai, L. Wang, G. Sun, Z. Zhang, X. Pan, J. Zhou and E. Xie, *Chem. Eng. J.*, 2017, **320**, 34.